

MQ NMR and SPME Analysis of Nonlinearity in the Degradation of a Filled Silicone Elastomer

Sarah C. Chinn,^{*,†} Cynthia T. Alviso,[†] Elena S. F. Berman,^{†,‡} Christopher A. Harvey,[†] Robert S. Maxwell,[†] Thomas S. Wilson,[†] Rebecca Cohenour,[§] Kay Saalwächter,^{||} and Walter Chassé^{||}

Lawrence Livermore National Laboratory, 7000 East Avenue, Livermore, California 94550, Honeywell Inc., Federal Manufacturing & Technologies, Kansas City Plant, Kansas City, Missouri 64141, and Institut für Physik, Martin-Luther-Universität Halle-Wittenberg, Betty-Heimann-Strasse 7, D-06120 Halle, Germany

Received: February 13, 2010; Revised Manuscript Received: May 21, 2010

Radiation-induced degradation of polymeric materials occurs through numerous, simultaneous, competing chemical reactions. Although degradation is typically found to be linear in adsorbed dose, some silicone materials exhibit nonlinear dose dependence due to dose-dependent dominant degradation pathways. We have characterized the effects of radiative and thermal degradation on a model filled-PDMS system, Sylgard 184 (commonly used in electronic encapsulation and in biomedical applications), using traditional mechanical testing, NMR spectroscopy, and sample headspace analysis using solid-phase microextraction (SPME) followed by gas chromatography/mass spectrometry (GC/MS). The mechanical data and ¹H spin-echo NMR spectra indicated that radiation exposure leads to predominantly cross-linking over the cumulative dose range studied (0–250 kGy) with a rate roughly linear with dose. ¹H multiple-quantum NMR spectroscopy detected a bimodal distribution in the network structure, as expected from the proposed structure of Sylgard 184. The MQ NMR spectra further indicated that the radiation-induced structural changes were not linear in adsorbed dose and that competing chain scission mechanisms made a greater contribution to the overall degradation process in the range of 50–100 kGy (although cross-linking still dominated). The SPME–GC/MS data were analyzed using principal component analysis (PCA), which identified subtle changes in the distributions of degradation products (the cyclic siloxanes and other components of the material) as a function of age that provide insight into the dominant degradation pathways at low and high adsorbed dose.

1. Introduction

Because of the chemical and physical nature of the polydimethylsiloxane backbone, silicone polymeric networks have served as near-ideal model systems for studying the influence of structure on the polymer chain dynamics and, thus, the mechanical properties of broad classes of polymer–filler composite systems, including micro- and nanocomposites. Studies of filled silicone elastomers comprise a large amount of the polymer literature, because of their versatility and ubiquitous presence in the industrial world, with applications to lithographic materials, insulators, and coatings. Although the effects of ionizing radiation on silicone polymers have been studied for over 50 years, there are still unresolved issues.^{1–5} Most work to date has studied ranges of adsorbed dose in which the effects on molecular weight, sol fraction, evolved gas, and so on are typically linear with dose. Further, a significant fraction of these studies have been performed on soluble polymer chains and not cross-linked networks. In many cases in which systems were studied past their gel point, insight into the effects of radiation were typically drawn from the study of the remaining

soluble fraction and not the direct study of the gel (i.e., the cross-linked fraction).

Similarly to that of most other polymeric materials, the degradation of silicone-based materials generally occurs by multiple competing chain-breaking (scission, unzipping, backbiting) or chain-forming mechanisms (i.e., H vs Y cross-linking through varying free-radical mechanisms), bonding to the filler matrix, and so on.^{1–4,6–15} For both thermally and radiatively induced degradation, multiple, competing reaction pathways can exist and occur simultaneously to varying extents depending on variables such as the total input energy, monomer types (i.e., stabilizing phenyl groups), additives (fillers, stabilizers, etc.), and network topology. The resulting effects on the polymer are the net effect of the reactions that have occurred. Thermal degradation typically follows standard kinetics of thermally activated processes, although with the complications caused by multiple allowable reaction pathways. In fact, experiments have observed a shift between dominant mechanisms [e.g., dominance of acid-catalyzed hydrolytic chain scission at low temperatures (<110 °C) and backbiting of free chain ends to form cyclic siloxanes at high temperatures (typically greater than 120 °C)].^{10–13,16} Radiation damage, however, has generally been observed to be linear in adsorbed dose over distinct dose ranges that depend on the structure and composition of the polymer composite, although a few studies have observed nonlinear behavior at sufficiently high adsorbed doses. Over extended dose ranges, the competition between these overlapping reactions can, however, lead to nonlinear behavior.^{1,2,4,6,17} Unfortunately, the

* Corresponding author. E-mail: chinn7@llnl.gov. Phone: 925-422-5514.

[†] Lawrence Livermore National Laboratory.

[‡] Current address: Los Gatos Research, 67 East Evelyn Ave., Ste. 3, Mountain View, CA 94041.

[§] Honeywell Inc.

^{||} Martin-Luther-Universität Halle-Wittenberg.

specific changes in the dominating mechanisms that might be responsible for this variance, particularly in radiation-induced degradation, are generally poorly understood. This is due in no small part to a lack of methodologies that provide correlations between changes in chemical speciation and the remaining composite network structure that determine the engineering properties.

Herein, we describe a general multipronged approach to developing improved insight into the chemical origins of degradation in a commercial silica-filled silicone polymer formulation that is broadly applicable to silicone-based materials. In this study, the effects of γ -radiation and exposure to elevated temperature are investigated as test cases using a combination of advanced ^1H multiple-quantum (MQ) NMR spectroscopy and solid-phase microextraction (SPME)–GC/MS. The benefits of MQ NMR spectroscopy lie in its ability to identify network-specific changes that are not available by other means and to enable the quantitative assessment of structural dynamics as a function of long-term exposure to chemically, thermally, or radiatively harsh environments.^{6–9} The MQ NMR growth curves were analyzed with the aid of new robust algorithms that dramatically reduce the variability in analyzing the results. Further, SPME–GC/MS has found great use in the identification of volatile offgassing components^{18,19} and previously has been used to identify the major byproducts of siloxane degradation,^{8,14,20} thus aiding in the elucidation of degradation mechanisms. Moreover, whereas the combination of SPME–GC/MS data sets with modern multivariate analysis methods has been used extensively in the food industry,^{21–24} its applicability to SPME analysis of silicone degradation has not yet been reported. Here, GC/MS chromatograms were analyzed by principal component analysis (PCA) to determine common signatures of aging mechanisms and to gain a complete understanding of degradation prevalence and pathways. Combined with traditional analysis, the MQ NMR and SPME–GC/MS results allowed the quantification of changes in the network structure and identification of responsible degradation mechanisms as a function of cumulative γ -radiation dose or temperature.

2. Experimental Section

2.1. Sample Preparation. Experiments were performed on samples of Sylgard 184, which, because of its versatile mechanical, chemical, and dielectric properties, has a number of other common uses, including in biomedical microelectromechanical system (MEMS) devices, in aerospace sealants, and use as a soft lithography material. Sylgard 184 is a platinum-catalyzed vinyl-addition silicone polymer manufactured by Dow Corning. The commercially available material consists of a 10:1 mixture of Sylgard 184 base resin and curing agent consisting of polymethylhydrosiloxane (PMHS) and polydimethylsiloxane (PDMS). The base resin is composed of ~65% vinyl-end-capped PDMS and ~35% soluble silica filler (50% SiO_2 , 45% trimethyl-end-capped PDMS, and 5% vinyl-end-capped PDMS) plus ~6 ppm chloroplatinic acid adduct as a catalyst. The samples were vacuum-degassed and cured for 7 days at room temperature.

Test samples were cut into strips and placed into aging containers that were either left open to air or backfilled with nitrogen. The samples were then exposed to ^{60}Co radiation at a dose rate of 0.5 kGy/h for times necessary to reach desired doses ranging from 10 to 250 kGy. After this aging, samples were further prepared and characterized as detailed below.

2.2. Mechanical and Rheological Testing. A TA Instruments Q1000 differential scanning calorimeter (DSC) was used to determine glass transition temperatures. Approximately

10–15 mg of sample was sealed in an aluminum pan. The samples were subjected to a modulated 1.5 °C/min temperature ramp from –160 to 50 °C with a temperature modulation of ± 0.27 °C every 20 s under a helium purge at a flow rate of approximately 50 mL/min.

Young's moduli for the Sylgard 184 material were determined using an MTS Synergie 400 tensile test frame equipped with a 50 N load cell. Test specimens were cut into strips that were approximately 30 mm long, 5 mm wide, and 1.5–2.2 mm thick. The specimen clamps were of screw type, and strain was measured based on grip separation, which limited measured properties to the initial modulus. Testing was carried out using an initial gauge length of 15 mm and at an initial strain rate of 0.5 min^{-1} , consistent with standard method ASTM D882-02. Reported results are the averages of three or four tests per condition.

2.3. NMR Experiments. **2.3.1. Correlation to Structural Parameters.** The residual dipolar couplings, $\langle\Omega_d\rangle$, are a result of incomplete motional averaging of magnetic dipole–dipole interactions due to structural variables within the polymer that lead to inhomogeneities in the motion of the monomers and prevent complete averaging to zero of the dipolar interactions. The correlation between residual dipolar couplings measured by NMR methods and structural variables has been reviewed in detail elsewhere and can be summarized in the following correlation between residual dipolar couplings; the dynamic order parameter, S_b ; and the number of statistical segments, N , between constraints^{25–30}

$$S_b = \frac{1}{P_2(\cos \alpha) \langle\Omega_d\rangle_{\text{static}}} = \frac{3r^2}{5N} \quad (1)$$

Here, the static dipolar coupling, $\langle\Omega_d\rangle_{\text{static}}$, is preaveraged by the rotation of the methyl groups in PDMS; $P_2(\cos \alpha)$ is the second-order Legendre polynomial describing the orientational changes between the dipolar vector and the chain axis; and r describes the distance relationship between the end-to-end vector, \mathbf{R} , and that of the unperturbed melt, \mathbf{R}_0 : $r = \mathbf{R}/\mathbf{R}_0$.³¹

2.3.2. NMR Methods. NMR experiments were performed on a Bruker Avance spectrometer with a proton Larmor frequency of 400.13 MHz. Pulse lengths of 90° with $\tau_p = 5.45 \mu\text{s}$ and recycle delays of 6 s were used. Traditional spin–echo experiments^{26,32} were fit to a bimodal distribution of decaying exponentials. The curves were characterized in all cases by a short- T_2 regime assigned to low-mobility network chains and a long- T_2 domain attributed to the non-network chains and chain ends that are located far from topological constraints. In this report, we have used the T_2 analysis primarily to obtain insight into the sol fraction. The long- T_2 fraction is actually made up of both the sol fraction and spins residing on the highly mobile ends of dangling chains, as discussed in Mayer et al. and Cohen-Addad, for example.^{26,33} Although a gross simplification, however, the relative amount of long- T_2 domains can be treated as proportional to the sol fraction, and relative fractional changes in the long- T_2 domains are thus related to the relative changes in sol fraction.^{2,4,8}

Multiple-quantum NMR experiments were performed as described by Saalwächter et al.^{31,34} using the generic pulse sequence to excite even-quantum coherences. The dipolar couplings contributing to the normalized double-quantum (DQ) buildup curve were fit as described in detail by Giuliani et al.¹⁵ and Saalwächter et al.^{31,34} using an inverted Gaussian of the form

$$I_{\text{nDQ}}(\langle\Omega_{\text{d}}\rangle; \tau_{\text{DQ}}) = 0.5 \left[1 - \exp\left(-\frac{2}{5} \langle\Omega_{\text{d}}\rangle^2 \tau_{\text{DQ}}^2\right) \right] \quad (2)$$

where $\langle\Omega_{\text{d}}\rangle$ is the average dipolar coupling and τ_{DQ} is the DQ mixing time described above. For bimodal distributions, a weighted sum of two inverted Gaussians in the form of eq 3 (see below) was used. In this experiment, attempts to fit buildup curves to inverted Gaussians with distributions of coupling frequencies, as described in earlier work,^{15,31} yielded nonphysical results. Instead, the fast Tikhonov regularization software FTIKREG was used to invert the distribution integral to estimate the distribution of coupling frequencies for each sample using eq 3 as a kernel function, as described previously, but with modifications as described in the next section.^{15,31,35}

2.3.3. Modified Regularization Process for MQ Data Analysis. In the original version of the modified regularization program for the estimation of coupling distributions, originally published by Weese,³⁵ eq 3 was used directly as a kernel function.³¹ This creates a problem in that the final normalized DQ intensity, which must always reach 0.5 in the long-time limit, had to be enforced by adding a few long-time data points with $I_{\text{nDQ}} = 0.5$ (particularly necessary because data are fitted only up to $I_{\text{nDQ}} = 0.45$, see below). Because FTIKREG was initially conceived for inverse Laplace transformations (i.e., just a falling exponential as a kernel function), it has a built-in option to enforce $I = 0$ in the long-time limit. To employ this option and obviate the use of an arbitrary number of additional points, the program now internally fits decay data of the form $0.5 - I_{\text{nDQ}}$ to a falling Gaussian, $0.5 \times \exp(-\frac{2}{5} \langle\Omega_{\text{d}}\rangle^2 \tau_{\text{DQ}}^2)$. In addition, we have implemented a new empirical kernel function

$$y = 0.5 \{ 1 - \exp[-(0.378 \times 2\pi \langle\Omega_{\text{d}}\rangle)^{15} \tau^{15}] \times \cos(0.583 \times 2\pi \langle\Omega_{\text{d}}\rangle \tau) \} \quad (3)$$

that includes the slight maximum observed in the normalized data and thus gives more reliable results for wider or multimodal distributions. Details will be reported in an upcoming publication.

We have also implemented changes in the error parameter that is required by FTIKREG. This parameter should reflect the constant, absolute-scale statistical error associated with the data points and is needed for the proper initialization of the regularization parameter. It affects the smoothing of the data and the number of distribution modes extracted from the data; regularization parameters that are too low commonly lead to an “overinterpretation” of the results in terms of too many modes. This is problematic for two reasons: First, the error increases for longer times (as the intensities become low) because of the normalization procedure needed to remove relaxation effects,³¹ thus rendering it nonconstant. Second, eq 3 is only an approximation of true data, which exhibits a weak maximum in narrowly distributed systems. This, in fact, is why data are fitted only up to $I_{\text{nDQ}} < 0.45$ (or, with our modified fit, down to 0.05), which is the region of good agreement. For broad distributions, the inability of eq 3 to model the maximum of the subcomponents leads to underestimations of more weakly coupled subcomponents.

To select an error parameter that leads to a physically realistic distribution, the program now automatically varies the error parameter over a variable range and outputs the distribution for each value, along with the corresponding χ^2 value (mean squared deviation between data and fit). See Figure 1A,B for the variation of χ^2 with the given error parameter and the resulting distributions. We take the most realistic distribution (shown in

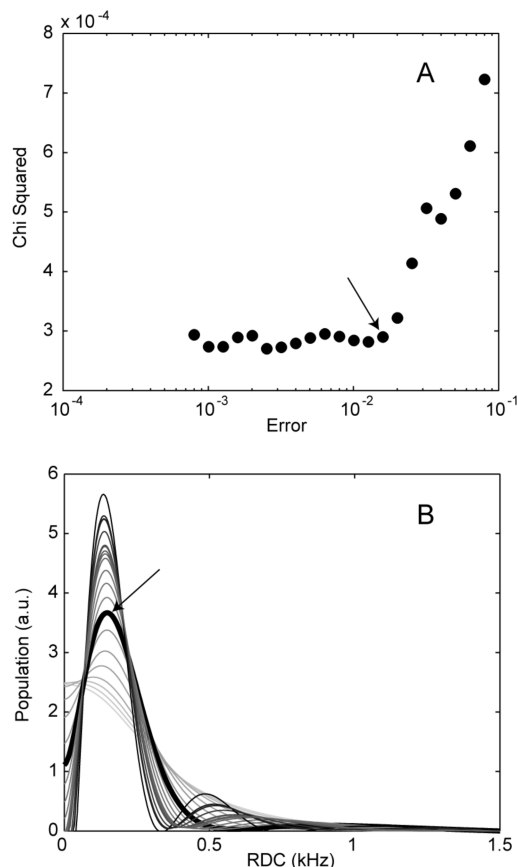


Figure 1. (A) χ^2 as a function of input error in the FTIKREG program. (B) Distributions of $\langle\Omega_{\text{d}}\rangle$ as a function of input error (and χ^2) for pristine Sylgard 184. The color of the line changes from black to lighter gray with increasing error. The arrows in the two panels indicate the chosen χ^2 value and distribution curve, with the appropriate distribution curve shown in bold.

bold in Figure 1) as the one for the lowest error parameter, below which χ^2 saturates at a nearly constant value. In most cases, much lower error values lead to multiply peaked distributions, which, however, do not lead to better overall fits and are consequently not necessarily physically meaningful.

2.4. Solid-Phase Microextraction–Gas Chromatography.

Carboxen/PDMS (85 μm) SPME fibers were purchased from Supelco. SPME headspace vials (20 mL), crimp caps, and septa (20 mm, Teflon/blue silicone, level 4) were purchased from MicroLiter Analytical Supplies. Three samples, weighing approximately 20–30 mg each, were placed in 20 mL SPME headspace vials. One set of Sylgard 184 samples (pristine and irradiated) was analyzed as-is, and one set was placed in a 70 $^{\circ}\text{C}$ oven for two weeks.

Headspace SPME analyses for a given radiation dose and temperature were performed on a blank control vial and on Sylgard 184. The samples were analyzed by SPME–GC/MS using an automated system under the following conditions: 85- μm Carboxen/PDMS SPME fiber, conditioned between samples for 5 min at 260 $^{\circ}\text{C}$; headspace sampled at 50 $^{\circ}\text{C}$ for 20 min and injected into the GC for 1 min at 250 $^{\circ}\text{C}$. The Agilent 6890 gas chromatograph was set for splitless injection and purged for 0.5 min using a J&W Scientific DB-624 column (30-m length, 0.25-mm i.d., 1.4- μm film) with a 1.0 mL/min constant flow of helium. The 20-min run had the following temperature profile: 40 $^{\circ}\text{C}$ /1.05 min, 23.41 $^{\circ}\text{C}/\text{min}$ to 260 $^{\circ}\text{C}$, and hold for 6.81 min. An Agilent 5973 mass spectrometer scanned the mass range from 35–450 at a rate of 1.81 scans/s with no filament

TABLE 1: Results of DSC, DMTA, Spin–Echo NMR Spectroscopy, and Two-Site Fit and FTIKREG Analysis of MQ Buildup Curves

dose (kGy)	T_g (°C)	G' (MPa)	$1/T_2$ (ms ^{−1})	two-site fit			FTIKREG			
				$\langle\Omega_d\rangle_1$ (Hz)	$\langle\Omega_d\rangle_2$ (Hz)	X_1 (%)	$\langle\Omega_d\rangle$ (Hz)	$\chi^2(\times 10^{-4})$	width (Hz)	relative width
0	−127.30	2.92	1.36	128.05	636.05	70.94	135.34	3.65	113	0.83
10	−127.26	2.92	1.36	135.11	679.60	74.34	145.36	2.90	118	0.81
50	−127.10	3.54	1.53	136.28	652.19	69.25	145.36	3.54	110	0.76
100	−126.99	5.08	1.80	160.79	792.31	67.90	190.48	8.45	148	0.78
250	−126.49	7.49	2.26	178.17	765.84	62.45	205.51	8.21	181	0.88

delay. Outgassing products were identified by comparison of their mass spectra to the NIST 02 mass spectral library.

2.4.1. Principal Component Analysis. PCA, a standard, unsupervised multivariate statistical technique, reduces a large data matrix to a few manageable variables that can be visualized and interpreted using a series of simple plots.^{36,37} PCA reduces the data complexity by calculating new variables called principal components, which represent linear combinations of the original variables and capture the greatest variation in the data set. The elution peaks and molecular fragments with the highest variance in intensity among the statistical groups identify important differences between samples.

GC/MS/MS spectra were aligned and analyzed using PLS Toolbox v. 4.1 (Eigenvector Research, Manson, WA) with MATLAB software v. 7.3 (MathWorks Inc., Natick, MA). The entire data set was first aligned to common peaks at 5.07, 6.75, 10.26, and 14.05 min utilizing a maximum allowable shift of 0.05 min for each of these reference peaks. Aligned individual spectra were normalized to unit area under the chromatogram, after which the entire data set was mean-centered. PCA was performed to reduce the complexity of the data set and aid in the identification of chemical species that changed significantly with treatment.

3. Results and Discussion

DSC, dynamic mechanical thermal analysis (DMTA), and spin–echo NMR spectroscopy were applied to the pristine and irradiated samples. The glass transition temperature, the Young's modulus, and the transverse relaxation rates ($1/T_2$) for both the long- T_2 and short- T_2 domains were seen to increase nearly linearly with adsorbed dose (data in Table 1). These results indicate a decrease in mobility with increasing radiation because of the dominance of cross-linking reactions expected for silicone materials.^{2,4,38} Extracted NMR-derived pseudosol fractions (see Experimental Section) decreased with increasing dose suggesting that radiation binds the small amount of sol component into the polymer network. The so-called Charlesby–Pinner plot of [sol fraction + (sol fraction)^{1/2}] vs $1/\text{dose}$ ^{39,40} is shown in Figure 2. The nonlinearity of the relationship is presumably due to the

large degree of structural heterogeneity in the PDMS network, but it might also reflect a transition in the dominant degradation mechanisms at about 50 kGy.³⁹ Extrapolation of the data to infinite dose yields a ratio of $G_s/G_c = 0.348$, where the G_i value is the number of chain-scission (s) or cross-linking (c) events per 100 eV of energy absorbed, indicating that cross-linking is roughly three times as likely to occur as chain scission.

Multiple-quantum growth curves were first fit to the discrete two-site model based on eq 3. The curves fit moderately well to the two-site model, which supports the suggestion by Schmid and Michel that Sylgard 184 behaves like a bimodal network.⁴¹ The two modes can be attributed to long, mobile PDMS chains with lower values of residual dipolar couplings (~ 130 Hz) and a mode comprised of short, less mobile PDMS chains, short hydrosilane cross-linkers, and polymer chains at or near the SiO₂ filler surface with higher $\langle\Omega_d\rangle$ values (~ 640 Hz). The exact couplings and fractions of chains in site 1 (low-frequency coupling mode) are shown numerically in Table 1. With increasing dose, a general increase in both the low-frequency and high-frequency sites was observed, although the high-frequency mode displayed some degree of nonlinearity in the increase, possibly because of imperfections in the fit. The majority of the chains were found to be in site 1 (low-frequency coupling mode), and the overall fraction increased between 0 and 10 kGy and then decreased at higher doses. This suggests an initial softening of the material followed by a gradual stiffening of the network and indicates a competition of at least two degradation mechanisms as suggested in the Charlesby–Pinner analysis. The initial softening followed by stiffening has previously been observed in other filled silicone elastomers⁸ and has been attributed to an initial delamination of the polymer–filler interface due to a decrease in the hydrogen bonds that are responsible for the strong surface interaction. At higher doses, the subsequent decrease in chains in site 1 can be assumed to be due primarily to increased cross-linking.

The distribution of $\langle\Omega_d\rangle$ values from the FTIKREG analyses of the samples is shown in Figure 3, and the average $\langle\Omega_d\rangle$ value, χ^2 , and width of the primary coupling mode are reported in Table 1. This analysis resulted in primarily one distribution attributed to the large quantity of mobile polymer chains, with evidence of a shoulder due to the lower-frequency coupling modes. The breadth of the distributions is ultimately due to the structural heterogeneity of the PDMS networks. The mean $\langle\Omega_d\rangle$ value was observed to increase slightly as a function of dose up to 50 kGy, followed by a larger jump to higher values at higher doses. The increase in $\langle\Omega_d\rangle$ is due to an increase in the average cross-link density of the material, again suggesting a dominance of radiation-induced cross-linking. The increase in the breadth of the distribution observed with increasing dose (simplistically calculated as the half-width at half-height of the $\langle\Omega_d\rangle$ distribution curve, included in Table 1) is ultimately due to an increase in molecular weight distribution and thus structural heterogeneity, which has been suggested to result from increased chain-scission

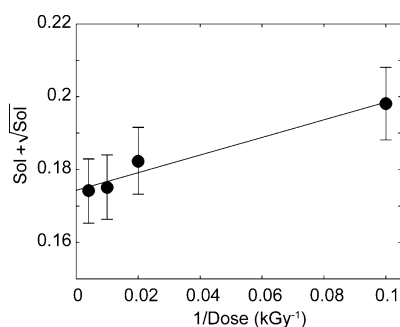


Figure 2. Charlesby–Pinner analysis by spin–echo NMR spectroscopy for irradiated Sylgard 184.

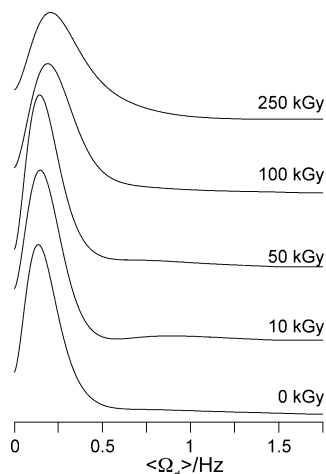


Figure 3. FTIKREG analysis of MQ growth curves for irradiated Sylgard 184.

events at higher dose.^{15,39} Additionally, the asymmetry in the distribution is due to an increase in the high-molecular-weight component that cannot be separated from the low-molecular-weight component because of the structural heterogeneity of these materials. However, the relative width, defined as the width divided by the mean $\langle \Omega_d \rangle$ value, appears to decrease up to 50 kGy and then increase at higher doses because of the increasing asymmetry of the distributions. The competition of mechanisms is manifest in the combined increase in the mean $\langle \Omega_d \rangle$ value and the broadening of the distribution width, although the data suggest that cross-linking is the dominant mechanism.

To obtain more information about the chemical nature of the changes observed as a function of radiation, headspace analysis was performed on the material. SPME–GC/MS analysis of the irradiated and thermally aged samples showed subtle trends in the total ion chromatographs, as demonstrated in Figure 4A for the irradiated samples and in Figure 4B for the irradiated samples further aged at 70 °C for two weeks. The major peaks are identified according to Table 2. Small changes in peak intensity can be seen for a few select peaks, but a detailed quantitative inspection of these changes would be difficult by traditional inspection methods. Note that traditional gases that evolve during irradiation, namely, hydrogen, methane, and ethane,^{1,3,5} were likely being produced but were not observed in our experimental design. The primary reasons for this are that these gases pass through the column too rapidly to be detected and, because the evolved gases are not being trapped during irradiation (only the gases evolving from the bulk sample during postirradiation analysis are being detected), the highly volatile, low-molecular-weight gas species are not, in fact, being sampled.

PCA of the irradiated samples that were analyzed without additional thermal aging is shown in Figure 5. Here, a plot of principal component 1 (PC1) vs principal component 2 (PC2) reveals distinct groupings for samples irradiated at different doses, indicating a discrete difference in offgassing signatures between the samples at each dose. Figure 6A shows the scores plot for PC1, which constitutes 49.03% of the overall variance in the samples, and shows a trend of decreasing scores with increasing radiation up to 50 kGy, followed by a leveling off of the scores. The loadings plot in Figure 6B indicates that the tetrahydrofuran (THF) peak at 5.43 min contributes most strongly to the positive scores (lowest doses), with a smaller contribution from butyrolactone (peak at 8.6 min), a common oxidation product of THF. The negative scores are due primarily

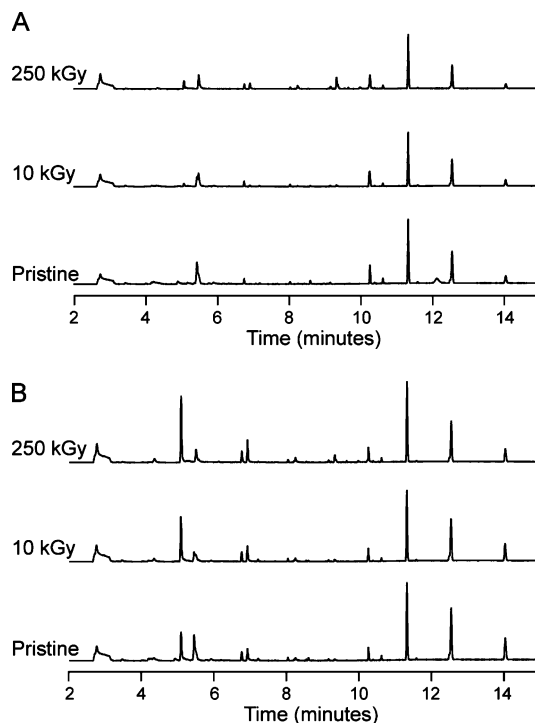


Figure 4. GC/MS total ion chromatograms from SPME headspace analysis of samples (A) irradiated and held at room temperature and (B) irradiated, then aged at 70 °C for two weeks.

TABLE 2: SPME–GC/MS Peak Assignments

elution time (min)	assignment
5.07	trimethylsilanol
5.43	tetrahydrofuran/acetic acid
6.91	<i>trans</i> -2(chlorovinyl) dimethylethoxysilane
8.23	cyclohexamethyltrisiloxane (d3)
8.60	butyrolactone
9.32	cyclo-octamethyltetrasiloxane (d4)
10.24	cyclodecamethylpentasiloxane (d5)
11.31	cyclododecamethylhexasiloxane (d6)
12.53	cyclotetradecamethylheptasiloxane (d7)
14.06	cyclohexadecamethyloctosiloxane (d8)

to the d4–d7 cyclic siloxanes [as well as residual peaks from the glass vials (present in the blank) at 2.7 min and from trimethylsilanol at 5.07 min], which are more prevalent for

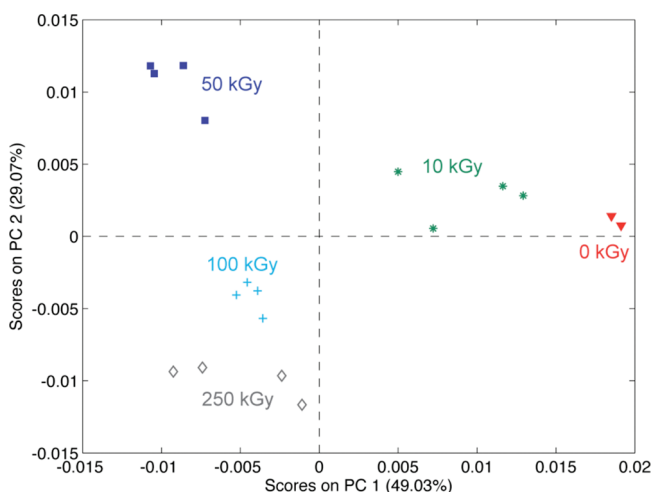


Figure 5. Principal component analysis of GC/MS data for samples irradiated and held at room temperature.

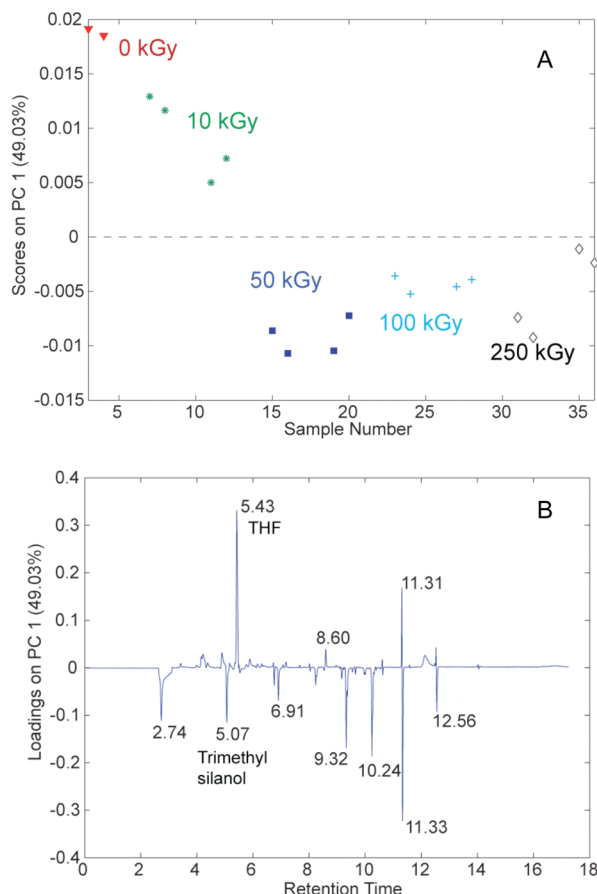


Figure 6. Plots of (A) scores and (B) loadings for principal component 1.

samples at higher radiation doses. An additional peak from *trans*-(2-chlorovinyl) dimethylethoxysilane at 6.91 min is presumed to be a reaction product from the catalyst, and its presence at higher doses suggests a possible postcure process occurring.

This analysis indicates that the changes in THF and butyrolactone concentrations are most significant at low doses. The overall THF signal concentration decreased with increasing dose, as can be seen by the slight decrease in signal intensity of the peak at 5.4 min in Figure 4A, although the overall effect is much more difficult to quantify on the total ion chromatogram (TIC). Between 10 and 50 kGy, there was a decrease in PC1 score that leveled off at higher doses. The negative scores seen here are primarily a result of changes in the d4–d7 cyclic siloxanes, as well as contributions from the trimethylsilanol peak at 5.07 min. The sudden decrease in PC1 score between 10 and 50 kGy as a result of the changes in cyclic siloxanes suggests an onset of backbiting chain-scission reactions that could result either in additional cross-linking sites within the network or in the generation of cyclic siloxanes. The competing mechanisms and the marked change in PC1 score confirm the observations from the MQ NMR analysis.

Analysis of PC2 (29.07% of the overall variance), shown in Figure 7, indicates a greater distinction between the behavior of the cyclic siloxanes. Positive loadings were present for the d5 and d6 cyclic siloxanes, with smaller positive loadings for acetic acid and the d7 and d8 cyclic siloxanes. The scores in Figure 7A increased with doses up to 50 kGy, and the corresponding loadings data indicate that the d5 and d6 cyclic siloxanes were the largest contributors to this increase. A large change in behavior was seen between 50 and 100 kGy, where

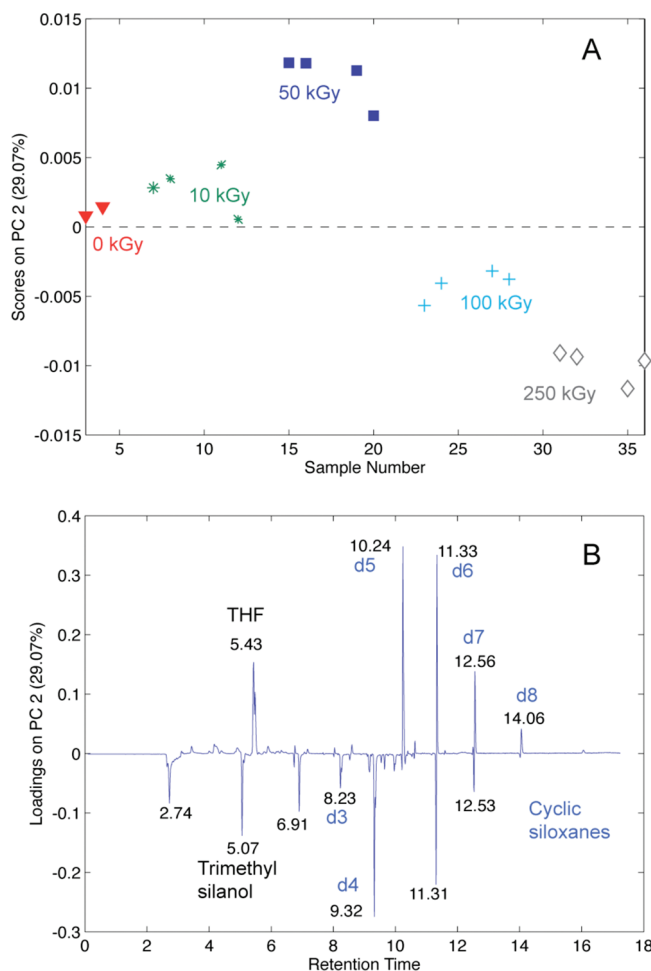


Figure 7. Plots of (A) scores and (B) loadings for principal component 2.

negative scores appeared, attributed mostly to the d3 and d4 cyclic siloxanes, trimethylsilanol, residual glass, and the catalysis byproduct. Unfortunately, the imperfect spectral alignment evident in Figure 7B hinders our ability to fully interpret the data, particularly for the d6 cyclic siloxane. However, the presence of the low-molecular-weight d3 and d4 cyclic siloxanes at the highest doses could be due to γ -irradiation-initiated polymerization reactions known to occur in such systems.^{42–44} Alternatively, the small amounts of chain-scission reactions that are competing with the cross-linking reactions could lead to backbiting reactions that form low-molecular-weight cyclic siloxanes.¹

When the already-irradiated samples were exposed to thermal degradation, a large amount of trimethylsilanol (peak at 5.06 min) was observed in the total ion chromatogram (Figure 4B). A scores plot of PC1 vs PC2 for all doses at both temperatures, shown in Figure 8A, indicates that the increased temperature had a far larger effect on the samples than any of the irradiation doses. Interestingly, the variance in the data that can be attributed to the increased temperature was far greater than any variance attributable to the radiation alone. Figure 8B shows the loadings plot for PC1, which represents 76.48% of the variance, with negative peak loadings correlated with room-temperature aging and positive loadings correlated with 70 °C aging. The large peak at 5.06 min is due to trimethylsilanol and was clearly the largest component contributing to the differences in the TIC signatures. The presence of this peak indicates a thermally induced process involving the trimethylsilanol end groups, which

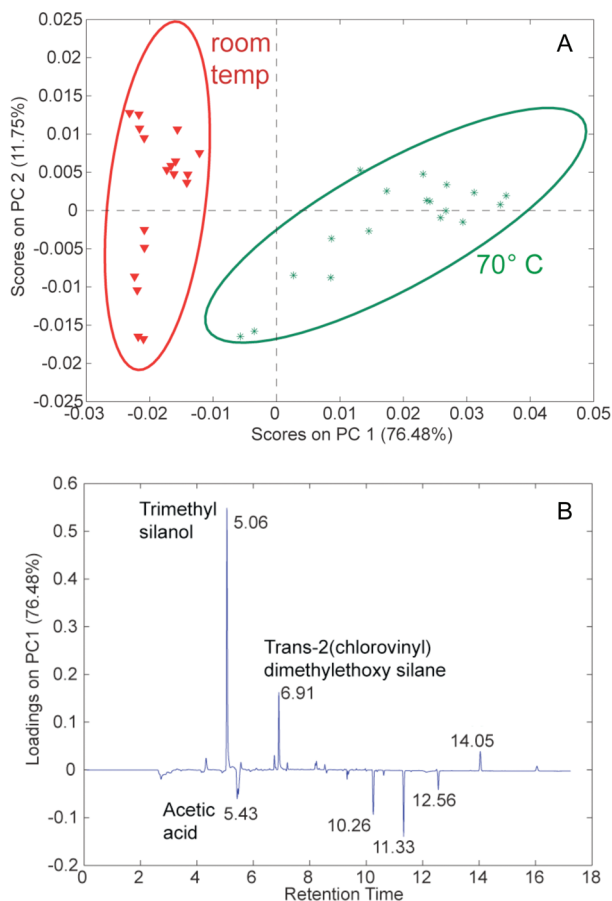


Figure 8. PCA plots comparing samples aged at 70 °C to those held at room temperature. (A) Scores plot for PC1 and PC2, (B) loadings plot for PC1. Ovals are 90% confidence ellipses.

are common products of hydrolytic chain scission. To a lesser extent, *trans*-(2-chlorovinyl) dimethylethoxysilane (peak at 6.91 min), the potential catalysis byproduct, appears to be more volatile at higher temperatures, as does a small amount of the d8 cyclic siloxane (14.05 min). The room-temperature samples, mainly characterized as having negative PC1 scores and loadings, are associated with an acetic acid peak at 5.43 min and the remainder of the cyclic siloxanes. It is interesting to note that the presence of trimethylsilanol was significantly greater than the relative amounts of cyclic siloxanes, which are commonly generated from backbiting chain-scission reactions. It is possible that the relatively low temperature of 70 °C is not enough to significantly degrade the samples in the traditional mechanism, although it is more likely that the total contribution of chain-scission mechanisms is simply producing smaller changes to the network structure than the removal of the trimethylsilanol groups.

The PCA analysis of the SPME–GC/MS data clearly indicates that, in the dose range of 50 kGy, a change in the dominant mechanisms has occurred. At low doses, limited damage was being done to the network, and the signatures observed were predominantly THF and THF oxidation products, although a number of cyclic siloxane and other synthesis byproducts of incomplete cure chemistry were observed at lower doses. As the dose was increased, radiation-induced chemistry began to contribute significantly to the evolved gas speciation. These reactions included postcuring reactions, radiatively induced cross-linking reactions that cleaved trimethylsilanol end groups, and radiation-induced chain scission. As the cross-link density increased with increasing damage, the relative rates of

creation of the various cyclic siloxane species changed, moving toward a preference for lower-molecular-weight cyclics, likely because of the increasingly restricted mobility of the network. The dramatic change observed in the PC1 and PC2 scores between 50 and 100 kGy occurred at the same doses in which the most significant change in both average residual dipolar coupling and distribution width occurred, again suggesting that the competition of cross-linking and chain-scission mechanisms is dose-dependent, with the dominance of cross-linking at the higher doses.

4. Conclusions

A comprehensive approach involving mechanical, rheological, spectroscopic, and chromatographic analyses to determine both physical and chemical changes to PDMS networks as a function of degradation mechanisms was presented. The effects of oxidative γ -radiation on Sylgard 184 were characterized with numerous analytical techniques to gain insight into the dependence on cumulative dose of the changes in segmental dynamics and mechanical properties of the material, as well as the speciation of volatile and semivolatile degradation products. Thermal analysis by DSC and DMTA indicated that there was a decrease in mobility as a result of radiation-induced cross-linking. NMR spin–echo experiments detected a decrease in sol fraction because of radiation-induced cross-linking. ^1H multiple-quantum NMR spectroscopy provided increased insight into the degradation effects on network structure, revealing the competition between cross-linking and chain-scission reactions. Headspace sampling from the bulk material followed by GC/MS analysis was performed at room temperature and elevated temperature to identify changes in outgassing species as a function of dose. Subsequent PCA was performed to assist in the analysis of the subtle changes in the GC/MS data. Although cross-linking was observed to dominate at all doses, at low doses (<50 kGy), a mechanism that favored higher-molecular-weight cyclic species and low-molecular-weight degradation products was dominant. At higher doses, the competition between cross-linking and chain scission increased, and backbiting reactions began to dominate, as reflected in the increased importance of lower-molecular-weight cyclic siloxanes. Further exposure to elevated temperature provided additional chain-scission opportunities, as evidenced by the significant offgassing of trimethylsilanol. Application of multivariate analysis afforded the ability to distinguish between the contributions of postcure reactions and those of other degradation mechanisms and also indicated a change in dominant mechanisms at around 50 kGy, consistent with the DSC and MQ NMR spectroscopy but not observed in the T_2 and DMTA analyses. The MQ NMR spectra and PCA analysis of the SPME data allowed for significantly enhanced insight into the chemical nature of radiation-induced degradation. Because typical predictions of long-term behavior often rely on extrapolations of changes in mechanical properties with degradation, without specific connection to the complex chemical changes that are causing such changes, erroneous long-term predictions of material performance are likely. Improved insight, as demonstrated in this study, provides the opportunity to improve lifetime predictions.

Acknowledgment. The authors acknowledge Jason Giuliani and Erica Gjersing for assistance with the implementation of the MQ NMR experiments at LLNL and James Lewicki for assistance in the GC/MS data interpretation. We also gratefully acknowledge Theresa Morris for assistance with the DSC analysis at KCP. This work was performed under the auspices

of the U.S. Department of Energy by Lawrence Livermore National Laboratory under Contract DE-AC52-07NA27344.

References and Notes

- (1) Aniruddha, S.; Clarson, S.; Widenhouse, C. *J. Inorg. Organomet. Polym.* **2008**, *18*, 207.
- (2) Charlesby, A. *Proc. R. Soc. London A* **1955**, *230*, 120.
- (3) Miller, A. *J. Am. Chem. Soc.* **1960**, *82*, 3519.
- (4) Charlesby, A.; Garratt, P. *Proc. R. Soc. London A* **1963**, *273*, 117.
- (5) Miller, A. *J. Am. Chem. Soc.* **1961**, *83*, 31.
- (6) Maxwell, R.; Balazs, B. *J. Chem. Phys.* **2002**, *116*, 10492.
- (7) Maxwell, R.; Cohenour, R.; Sung, W.; Solyom, D.; Patel, M. *Polym. Degrad. Stab.* **2003**, *80*, 443.
- (8) Chien, A.; Maxwell, R. S.; Chambers, D.; Balazs, B.; LeMay, J. J. *Radiat. Phys. Chem.* **2000**, *59*, 493.
- (9) Maxwell, R.; Chinn, S. C.; Solyom, D.; Cohenour, R. *Macromolecules* **2005**, *38*, 7026.
- (10) Grassie, N.; MacFarlane, I. *Eur. Polym. J.* **1978**, *14*, 875.
- (11) Grassie, N.; MacFarlane, I.; Francey, K. *Eur. Polym. J.* **1979**, *15*, 415.
- (12) Camino, G.; Lomakin, S.; Lazzari, M. *Polymer* **2001**, *42*, 2395.
- (13) Camino, G.; Lomakin, S.; Lageard, M. *Polymer* **2002**, *43*, 2011.
- (14) Hall, A.; Patel, M. *Polym. Degrad. Stab.* **2006**, *91*, 2532.
- (15) Giuliani, J. R.; Gjersing, E. L.; Chinn, S. C.; Jones, T. V.; Wilson, T. S.; Alviso, C. T.; Herberg, J. L.; Pearson, M. A.; Maxwell, R. S. *J. Phys. Chem. B* **2007**, *111*, 12977.
- (16) Patel, M.; Soames, M.; Skinner, A.; Stevens, T. S. *Polym. Degrad. Stab.* **2004**, *83*, 111.
- (17) Stevenson, I.; David, L.; Gauthier, C.; Arambourg, L.; Davenas, J.; Vigier, G. *Polymer* **2001**, *42*, 9287.
- (18) Hakkarainen, M.; Groning, M.; Albertsson, A. C. *J. Appl. Polym. Sci.* **2003**, *89*, 867.
- (19) Hakkarainen, M. *Adv. Polym. Sci.* **2008**, *211*, 23.
- (20) Maxwell, R. S.; Chinn, S. C.; Alviso, C. T.; Harvey, C. A.; Giuliani, J. R.; Wilson, T. S.; Cohenour, R. *Polym. Degrad. Stab.* **2009**, *94*, 456.
- (21) Mildner-Szkudlarz, S.; Jelen, H. H. *Food Chem.* **2008**, *110*, 751.
- (22) Korhonova, M.; Hron, K.; Klimcikova, D.; Muller, L.; Bednar, P.; Bartak, P. *Talanta* **2009**, *2009*, 710.
- (23) Mildner-Szkudlarz, S.; Jelen, H. H. *J. Food Qual.* **2010**, *33*, 21.
- (24) Jurado, J. M.; Ballesteros, O.; Alcazar, A.; Pablos, F.; Martin, M. J.; Vilchez, J. L.; Navalon, A. *Anal. Bioanal. Chem.* **2008**, *390*, 961.
- (25) Saalwächter, K.; Herrero, B.; Lopez-Manchado, M. *Macromolecules* **2005**, *38*, 9650.
- (26) Cohen-Addad, J. P. *Prog. NMR Spectrosc.* **1993**, *25*, 1.
- (27) Callaghan, P. T.; Samulski, E. T. *Macromolecules* **2000**, *33*, 3795.
- (28) Grinberg, F.; Kimmich, R.; Moller, M.; Molenberg, A. *J. Chem. Phys.* **1996**, *105*, 9657.
- (29) Schneider, M.; Gasper, L.; Demco, D. E.; Blumich, B. *J. Chem. Phys.* **1999**, *111*, 402.
- (30) Saalwächter, K. *Prog. NMR Spectrosc.* **2007**, *51*, 1.
- (31) Saalwächter, K.; Ziegler, P.; Spyckerelle, O.; Haider, H.; Vidal, A.; Sommer, J.-U. *J. Chem. Phys.* **2003**, *119*, 3468.
- (32) Mehring, M. *Principles of High Resolution NMR in Solids*; Springer-Verlag: Berlin, 1983.
- (33) Mayer, B. P.; Chinn, S. C.; Maxwell, R. S.; Reimer, J. A. *Chem. Eng. Sci.* **2009**, *64*, 4684.
- (34) Saalwächter, K. *J. Chem. Phys.* **2004**, *120*, 454.
- (35) Weese, J. *Comput. Phys. Commun.* **1992**, *69*, 99.
- (36) Jolliffe, I. T. *Principal Component Analysis*, 2nd ed.; Springer-Verlag: New York, 2002.
- (37) Jackson, J. E. *A User's Guide to Principal Components*; John Wiley & Sons: Hoboken, NJ, 2003.
- (38) Dawes, K.; Glover, L. In *Physical Properties of Polymers Handbook*; Mark, J., Ed.; American Institute of Physics: Woodbury, NY, 1996; p 557.
- (39) Saito, O.; Kang, H. Y.; Dole, M. *J. Chem. Phys.* **1967**, *46*, 3607.
- (40) Charlesby, A.; Pinner, S. H. *Proc. R. Soc. London A* **1959**, *249*, 367.
- (41) Schmid, H.; Michel, B. *Macromolecules* **2000**, *33*, 3042.
- (42) Lawton, E. J.; Grubb, W. T.; Balwit, J. S. *J. Polym. Sci.* **1956**, *19*, 455.
- (43) Wolf, C. J.; Stewart, A. C. *J. Phys. Chem.* **1962**, *66*, 1119.
- (44) Chawla, A. S.; St. Pierre, L. E. *J. Appl. Polym. Sci.* **1972**, *16*, 1887.

JP1013797